The Effects of Dust Optical Properties on the Scattering-induced Disk Polarization by Millimeter-sized Grains

Haifeng Yang[1,3] and Zhi-Yun Li[2]

[1] Institute for Advanced Study, Tsinghua University, Beijing, 100084, People's Republic of China; yanghaifeng@tsinghua.edu.cn
[2] Department of Astronomy, University of Virginia, Charlottesville, VA 22904, USA

Abstract

Spatially resolved (sub)millimeter polarization has been detected by Atacama Large Millimeter/submillimeter Array in an increasing number of disks. The majority of the observations show polarization patterns consistent with self scattering, especially at Band 7. The inferred sizes of the grains are typically of order 100 μm, which is very different from the millimeter size commonly inferred from the dust opacity index β. In an effort to resolve this discrepancy, we first introduce the so-called "Coplanar Isotropic Radiation Field" approximation, which enables the computation of the (signed) polarization fraction semianalytically. With an oft-adopted dust composition, we find that models with big dust grains produce very small polarization with reversed orientation, which has not been observed. The semianalytic results are validated through Monte Carlo radiative transfer simulations. In these models, the "correct" polarization orientation and the small β index are mutually exclusive. To resolve this tension, we explore a wide range of dust models, parameterized by their complex refractive indices $m = n + ik$. We find that both the fraction and the orientation of the polarization depend on the refractive index in a complex way, and this dependence is mapped out on an n–k plane for a representative 3 mm size distribution and wavelength of 870 μm. In particular, 3 mm-sized refractory organics grains produce reversed polarization, whereas grains made of absorptive carbonaceous materials produce a percent-level, nonreversed polarization; the latter may alleviate the aforementioned tension in grain size estimates. We conclude that scattering-induced polarization has the potential to also probe the grain compositions.

Unified Astronomy Thesaurus concepts: Protoplanetary disks (1300); Dust continuum emission (412); Circumstellar dust (236)

1. Introduction

Magnetic fields play a crucial role in the evolution and dynamics of an accreting protoplanetary disk, through either magnetorotational instability (Balbus & Hawley 1991) or magnetically driven wind (Blandford & Payne 1982). Direct evidence for the magnetic field in the disk, however, has been lacking.

Polarized light in the (sub)millimeter wavelengths has been established as a promising tool in probing celestial magnetic fields on larger scales ($\gtrsim$1000 au), from molecular clouds (Planck Collaboration et al. 2015; Fissel et al. 2016), to star-forming cores (see, e.g., reviews by Pattle & Fissel 2019 and Hull & Zhang 2019). However, when it comes to the disk scale (~100 au or less), the picture becomes more complicated. The very first resolved polarization map of a classical T Tauri disk using the Combined Array for Research in Millimeterwave Astronomy, reveals a uniform polarization pattern which would imply an unphysical magnetic field configuration in a differentially rotating system (Stephens et al. 2014). Since then, and thanks to the Atacama Large Millimeter/submillimeter Array (ALMA), many disk polarization maps have been made, leading to rapid observational progress in the field. The origins of these disk polarizations, however, remain unclear. Alongside the classical magnetic alignment interpretation, there exist at least three alternatives, scattering-induced polarization, radiative alignment, and mechanical alignment.

Although each one of the four aforementioned mechanisms has some observational support in certain systems, there is not

a single mechanism that can explain all observed polarization in protoplanetary disks. Alignment with respect to the local radiation anisotropy ("k-RAT alignment" thereafter) is best supported by the azimuthal polarization pattern observed at ALMA Band 3 in the HL Tau system (Kataoka et al. 2017). However, it predicts a strong azimuthal variation of polarization and circular pattern (rather than elliptical pattern) (Yang et al. 2019). There is some tentative evidences for alignment with respect to the magnetic field, through either Radiative Alignment Torques ("B-RAT alignment"; Lazarian & Hoang 2007), or recently proposed Mechanical Alignment Torques (Hoang et al. 2018), in, e.g., the IRAS 4A system at cm wavelengths (Cox et al. 2015; Yang et al. 2016b) and BHB07-11 (Alves et al. 2018) at (sub)millimeter wavelengths. But there is no well-resolved system that matches the theoretical expectations (see, e.g., Cho & Lazarian 2007; Yang et al. 2016b; Bertrang et al. 2017) assuming the widely expected disk toroidal magnetic field yet (Flock et al. 2015). Mechanical alignment has recently received some attention. Hoang et al. (2018) claims that under MATs, grains can be aligned with respect to local dust-gas streaming direction, in the case of a weak or zero magnetic field, even if the velocity difference is sub-sonic. Within this picture, Kataoka et al. (2019) investigated the direction of streaming velocities for dust grains with different Stokes numbers, and the resulting polarization orientations. They found that their polarization pattern in the order-of-unity Stokes number case resembles that observed by Alves et al. (2018) in BHB07-11. The BHB07-11, however, is a binary system, and we expect more complicated velocity fields than the simple one assumed in Kataoka et al. (2019). Yang et al. (2019) investigated the observational features of

---

[3] C.N. Yang Junior Fellow.

another mechanical alignment mechanism, the Gold mechanism (Gold 1952), to address the circular versus elliptical pattern problem in the ALMA Band 3 polarization observations of HL Tau disk. However, they failed to explain the nonexistence of strong azimuthal variation, and suggested the scattering by dust grains aligned under the Gold mechanism may be the origin of the polarization at ALMA Band 3 in the HL Tau system.

The scattering-induced polarization is quite different from alignment-based mechanisms discussed above. It is the mechanism that has the strongest observational support so far. Soon after it was initially proposed by Kataoka et al. (2015), Yang et al. (2016a) first pointed out that self scattering in the Rayleigh regime will produce uniform polarization patterns in an inclined disk system (see also Kataoka et al. 2016 and discussions in Section 2.1). This uniform polarization pattern has been observed in many systems, with HL Tau (Stephens et al. 2017), and IM Lup (Hull et al. 2018), and HD 163296 (Dent et al. 2019) as the best and well-resolved examples, plus many others, e.g., DG Tau (Bacciotti et al. 2018), HH80/81 (Girart et al. 2018), VLA1623 (Harris et al. 2018), HH 111 and HH 212 (Lee et al. 2018), and RY Tau (Harrison et al. 2019). The predicted (and observed) uniform polarization pattern is almost impossible to produce for any alignment-based mechanism. These alignment-based mechanisms rely on the dichroic emission of aspherical dust grains aligned with respect to some sort of local field, e.g., the magnetic field, which is usually varying its direction in a rotating protoplanetary disk. At this time, the observed uniform polarization pattern is a feature unique to the scattering-induced polarization, and the wide-spread detection of such a pattern is a strong evidence for the mechanism.

Despite the success of the scattering-induced polarization, it is in serious tension with previous work using the "β index" to probe grain sizes (see PPVI review by Testi et al. 2014 and references therein; see also Carrasco-González et al. 2019). Thanks to the strong dependence of scattering opacity on grain sizes, one can probe the grain sizes in protoplanetary disks. To reproduce the observed polarization fraction at ALMA Band 7 ($\sim$870 μm), the optimal grain size is about $\sim$140 μm when the size parameter ($x \equiv 2\pi a/\lambda$) is on order of unity. Previous work using this method all found grain sizes not too far from this value ($\sim$100 μm; Kataoka et al. 2016; Yang et al. 2016a; Hull et al. 2018; Dent et al. 2019).

On the other hand, the well-established "β index" method can probe the grain size in protoplanetary disk independently. If the inferred opacity index β is smaller than 1 in a system at a certain wavelength λ, the emission at that wavelength should be dominated by grains of at least 3λ in size (Draine 2006; Testi et al. 2014). Small opacity index β at millimeter wavelengths can then serve as a probe for big dust grains with sizes of millimeters or even centimeters (e.g., Pérez et al. 2012, 2015). For example, ALMA Partnership et al. (2015) reported resolved β index in HL Tau disk with values mostly smaller than one between ALMA Band 7 ($\sim$0.87 mm) and Band 6 ($\sim$1.3 mm), which would require grains of at least $\sim$3 mm in size.[4]

This discrepancy in the grain sizes estimated from the scattering and "β index" methods needs to be resolved before we can use either method to probe the grain growth in protoplanetary disks with confidence. Obviously, one (or both) of the two methods need to be modified to agree with the other. In this paper, we will assume that the opacity index β is indeed small and that the small β comes from big dust grains, and focus on understanding the role of such grains in producing polarization at shorter wavelengths through scattering.

Our most important conclusion will be that millimeter-sized grains can produce percent-level polarization along the disk minor axis at relatively short wavelengths, particularly 870 μm (ALMA Band 7), if their optical properties (specifically complex refractive index) fall in certain parameter regime (see Figure 4 in Section 4). This conclusion is drawn using an approximate semianalytic method (under the so-called "coplanar isotropic radiation field" approximation) for computing disk polarization that allows for efficient exploration of parameter space. This method was introduced by Yang et al. (2016b) and was closely related to that used in Kataoka et al. (2015); it is described in Section 2.1. It is checked against a Monte Carlo-based method (described in Section 2.2) which is more general but more time consuming. In addition, the second method yields the spectral index and polarization map of the disk that are not available from the first method and that can aid in illustrating the problem under consideration and interpreting the results. This is followed by an explicit demonstration of the main problem that we seek to address, namely, the inability of grains of a commonly adopted composition (used by, e.g., DSHARP Birnstiel et al. 2018) to simultaneously explain the percent-level polarization often observed along the disk minor axis and the relatively low spectral index of dust emission, using both methods. In Section 4, we map out the parameter space in the "phase diagram" of the dust complex refractive index where this problem can be resolved. A specific example of the grains in this desired parameter space is given in Section 5, together with a discussion of the effects of the grain size distribution and the implications and limitations of this work. Finally, we give a summary in Section 6.
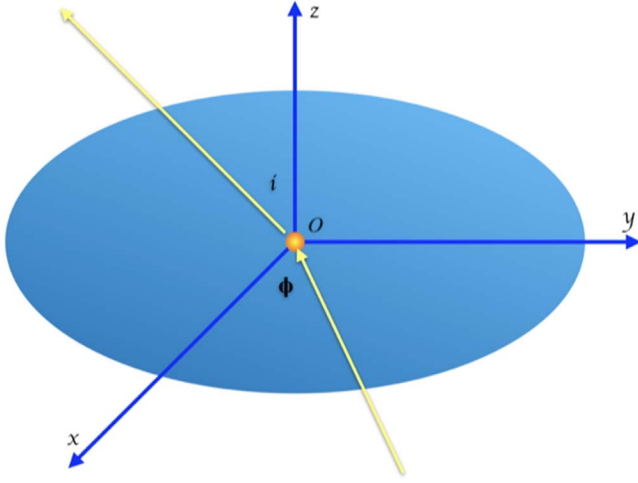
2. Method

2.1. Coplanar Isotropic Radiation Field

Scattering-induced polarization at (sub)millimeter wavelengths is very different from polarization at infrared caused by dust scattering in, e.g., reflection nebulae. The major difference is that the photons at these wavelengths are dust thermal emission to begin with. When studying the polarization from such self-scattering events, one need to, in principle, consider the dust grains in the whole disk. However, even without a global disk model, we can still study the polarization from scattering with the local Coplanar Isotropic Radiation Field (CIRF hereafter) approximation. This approximation was first introduced in Yang et al. (2016a), together with Rayleigh scattering approximation in the small particle limit.[5] Because it lies at the heart of this work, we will describe the approximation in detail in the following while relaxing the assumption of small dust grains.

Let the scatterer be at the origin O of our Cartesian coordinate system (see Figure 1). We have the disk on the xOy

---

[4] We caution that care must be exercised when inferring the opacity index β from the observed spectral index α, especially from relatively low-resolution observations of highly structured disks that can blend together the emission from optically thin gaps and optically thick rings to yield apparently low values of β, as pointed out by, e.g., ALMA Partnership et al. (2015; see Lin et al. 2020 for an explicit illustration of this effect).

[5] The CIRF approximation is appropriate near the disk center and in regions of the disk that are optically thick along the disk plane.

Figure 1. Geometry adopted. A spherical scatterer is placed at the center of the coordinate. It is illuminated by unpolarized radiation confined to the xOy plane. The line of sight lies in the xOz plane and has an inclination angle i with the z axis.

plane. The question is, what is the polarization state of the light scattered by this particle, when viewed from a line of sight (LOS) l in the xOz plane with an inclination angle i with respect to the symmetry axis of the disk z. The sky plane is then a plane perpendicular to this direction. In general, we need to consider the incoming light from all solid angles. In this problem of our interest, we can instead consider only those coming from particles sitting right on the disk midplane, the xOy plane. To describe any incoming light, one then need only one argument ϕ, the angle between the negative direction of the incoming light and the x axis. Note that the xOy plane, or the disk plane, shares one line with the sky plane: the y axis. If we put a circle in the xOy plane, it will be projected to the sky plane as an ellipse. This y axis will then be the major axis of this ellipse. A direction perpendicular to both y axis and the LOS is then the direction of the minor axis of the ellipse.

We will use Stokes vector $\boldsymbol{S} \equiv (I, Q, U, V)$ to describe the polarization state of the light, and further assume all incoming radiation is unpolarized. This is valid as long as the grains are spherical or not aligned and secondary effects from multiple scattering events are negligible. This assumption helps us focus on understanding the scattering problem, without the complication from grain alignment. Under these assumptions, the Stokes I of the scattered light can be expressed as[6]

$$I \propto \int_0^{2\pi} Z_{11}(\theta_s(\phi))\,d\phi, \qquad (1)$$

where θ_s is the scattering angle (i.e., the angle between the incoming and scattered light). For the adopted setting, we have $\cos\theta_s(\phi) = -\sin i \cos\phi$. Z_{ij} is the Muller matrix, with Z_{11} being the component that relates the incoming Stokes I with the scattered Stokes I. Once given the dielectric function and the grain size parameters $x \equiv 2\pi a/\lambda$, the Muller matrix can be calculated through the Mie theory (Bohren & Huffman 1983), assuming compact spherical dust grains.

---

[6] This can be made more rigorous with the aid of Dirac δ function. In this work, we only care about the ratio of the Stokes I and Q of the scattered light. So the same factor in the front can be safely ignored. For examples of more rigorous formulae, see Yang et al. (2016a).

The expressions for Stokes Q and U are more complicated:

$$Q \propto \int_0^{2\pi} Z_{21}(\theta_s(\phi))\cos(2\phi'(\phi))\,d\phi, \qquad (2)$$

$$U \propto \int_0^{2\pi} Z_{31}(\theta_s(\phi))\sin(2\phi'(\phi))\,d\phi, \qquad (3)$$

where the Stokes Q has been defined such that $Q = I$ implies fully polarized light along x'-direction, the direction of x axis projected to the sky plane (i.e., the minor axis of an inclined disk). ϕ' is the angle ϕ (between the x axis and the incoming light, see Figure 1) projected onto the sky plane. The extra trigonometric function factors with the argument $2\phi'$ (compared with Equation (1)) are due to the translation of Stokes vectors from the scattering frame to the lab frame. It describes how the scattered light originating from different incoming directions contributes to the polarization of the scattered light. For the adopted geometry, we have

$$\cos(\phi'(\phi)) = -\frac{\sin\phi}{\sqrt{\cos^2 i \cos^2\phi + \sin^2\phi}},$$

$$\sin(\phi'(\phi)) = \frac{\cos i \cos\phi}{\sqrt{\cos^2 i \cos^2\phi + \sin^2\phi}}. \qquad (4)$$

We can easily check that $\sin(2\phi'(\phi)) = -\sin(2\phi'(-\phi))$. At the same time, $\theta_s(\phi) = \theta_s(-\phi)$. So we have $U = 0$, regardless of the Muller's matrix. This is expected due to the symmetry of our setting.

The polarization fraction of the scattered light is given by

$$p_s = \frac{\int_0^{2\pi} Z_{21}(\theta_s(\phi))\cos(2\phi'(\phi))\,d\phi}{\int_0^{2\pi} Z_{11}(\theta_s(\phi))\,d\phi}. \qquad (5)$$

We have defined the Stokes Q such that a negative p_s means the polarization is along the y axis, i.e., the major axis of the disk (see discussions above). A positive p_s then gives a polarization along the minor axis of the disk (i.e., the x' direction, which is the x axis projected onto the sky plane).

In the limit of Rayleigh scattering, one recovers the following expression for scattering-induced polarization (see also Equation (18) in Yang et al. 2016a):

$$p_s = \frac{\sin^2 i}{2 + \sin^2 i}. \qquad (6)$$

For the rest of this paper, we will consider $45°$ as a representative inclination angle. At this inclination angle, Rayleigh scattering gives $p_s = 0.2$, which means 20% of the scattered light is polarized. Note that this does not mean the polarization from self scattering is as high as 20%. One need to take into account the albedo and the disk structure (see Section 3 for more detailed discussion) to determine the polarization fraction in a disk.

2.2. Fiducial Disk Model and Monte Carlo Radiative Transfer

To verify the results obtained with the semianalytic CIRF method, we also conduct Monte Carlo Radiative Transfer calculations with publicly available RADMC-3D code (Dullemond et al. 2012). To do so, one need a dust model and a disk model (a density distribution and a temperature distribution). The dust model can be described by its dielectric function and a grain size

distribution. These will be discussed in more detail later. We will first introduce our fiducial disk model, which applies to all calculations in this paper.

The disk model we adopt is the one used in Hull et al. (2018) for IM Lup. This is one of the best modeled scattering-induced polarization to date (see comparison between Figure 4 and Figures 1–3 in Hull et al. 2018). This model is a modified version of Cleeves et al. (2016), which is a viscous disk (Lynden-Bell & Pringle 1974) described by

$$\Sigma = \Sigma_c \left(\frac{R}{R_c} \right)^{-\gamma} \exp\left[-\left(\frac{R}{R_c} \right)^{\alpha} \right], \tag{7}$$

where $\Sigma_c = 25$ g cm^{-2} is the column density for gas, and a gas-to-dust ratio of 100 is adopted. $R_c = 100$ au is a characteristic radius. The power-law index for column density $\gamma = 0.3$. In the vertical direction, the disk is set to be in hydrostatic equilibrium with a midplane temperature prescribed as

$$T_m = T_0 \left(\frac{R}{R_c} \right)^{-q}, \tag{8}$$

where $T_0 = 70$ K and $q = 0.43$. We further reduce the scale height of the dust by a factor of 20, as we expect them to be well settled toward the disk midplane (e.g., the HL Tau disk thickness has been estimated to be thinner than 1 au by Pinte et al. 2016). The near-far side asymmetry in the polarized intensity predicted for optically and geometrically thick disks are generally not observed in late type T Tauri systems with ordered polarization maps, which also implies geometrically thin disk (Yang et al. 2017).

The MC Radiative Transfer calculations are done on a spherical-polar coordinate system. The radial grid is logarithmically spaced between 5 and 200 au with 150 cells in between. The θ grid is uniformly spaced in a wedge with 64 cells and a half opening angle of 0.07 radian. This gives about 5.8 scale heights on both sides of the disk at R_c. The ϕ grid spans 0 to 2π uniformly with 64 cells. For each MC run, we use 5×10^9 photon packages.

Ideally, one would like to calculate the temperature profile self consistently. However, the detailed temperature profile strongly depends on the amount of small dust grains and the spatial distribution of them, which reprocess the starlight. At the same time, the observed polarization at (sub)millimeter emission is mostly contributed by large dust grains near the midplane of the disk. The small dust grains have limited contribution to the observed thermal emission beyond the effects on the temperature. These two species of dust grains are not directly connected to each other. One has to make some assumptions to connect them together, or prescribe them separately. For example, one can assume a simple power-law model, or assume more complicated distributions such as the steady-state solution of grain coagulation and fragmentation (Birnstiel et al. 2012). One can also split these two species completely and have the small dust grains mixed with gas and large dust grains settled toward the mid plane (e.g., Cleeves et al. 2016). Once the dust distribution is prescribed, the temperature distribution can be calculated with the Monte Carlo method, self consistently. This process, however, is more computational expensive and is not much better than simply prescribing a temperature distribution because one can change

the temperature distribution by changing the distribution of the small grains, which is generally not well constrained observationally.

On the other hand, the Monte Carlo method discussed in this subsection is only for illustrative purposes to verify our conclusions from the semianalytical model and produce spatial distributions of the polarization properties, such as orientation and polarization fraction. The expensive Monte Carlo calculation of the dust temperature is not necessary for this purpose.
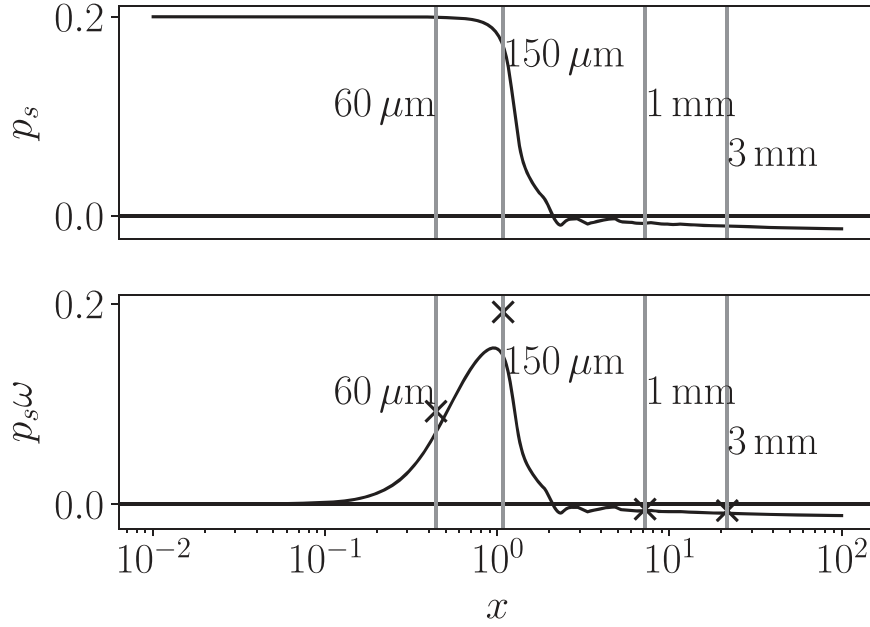
3. Scattering by Large Grains of DSHARP Composition

3.1. Low Polarization Fraction and Potential Polarization Reversal

With the two methods established, we are now in a good position to study the polarization produced by the big dust grains through scattering in an inclined disk. We will focus on the 870 μm wavelength, which is the ALMA Band 7. This is the shortest wavelength that ALMA can detect dust polarization at and is where the clear uniform polarization patterns, which are strong signatures of scattering-induced polarization, are observed most frequently (Stephens et al. 2017; Bacciotti et al. 2018; Hull et al. 2018; Dent et al. 2019). At this wavelength, disk polarization has often been attributed to the self scattering of $\sim$100 μm dust grains. Such grains are too small to produce the small opacity index β ($\lesssim$1) that is often inferred at millimeter wavelengths.

For the dust composition, we adopt the dust mixture used in the DSHARP project (Birnstiel et al. 2018). It is a mixture of water ice (Warren & Brandt 2008), refractory organics (Henning & Stognienko 1996), troilite (Henning & Stognienko 1996), and astronomical silicate (Draine 2003). The mass fractions are 0.2, 0.3966, 0.0743, and 0.3291, respectively. We will focus on one dust composition in this section and vary the grain sizes to understand the effects of grain sizes. In Section 4, we will relax this assumption and explore the polarization produced by dust grains with different compositions.

We will further assume a power-law grain size distribution with a power-law index of -3.5 (Mathis et al. 1977; MRN distribution hereafter). A distribution of grains with different sizes, as oppose to single-sized grains, will help avoiding strong oscillations (in both the phase function and in the opacities as functions of grain sizes) when the size parameter is on the order of unity. Other power laws will be considered in Section 5.1.

With the dust composition given, we can calculate the Muller Matrix through the Mie theory, assuming compact spherical dust grains. We then calculate the polarization from scattering in an inclined disk numerically through Equation (5). We will use a fiducial inclination angle 45° throughout this paper. The upper panel of Figure 2 shows the (signed polarization fraction) p_s for different grain sizes in terms of the dimensionless size parameter. We can see that the polarization is constant at 20% for small dust grains, but drops very quickly as x increases beyond unity, with some oscillations as it drops. Both the decrease and oscillation are due to different parts of the dust grains having different phases during the scattering. Interestingly, we find that for big dust grains, the polarization fraction became negative which, for a disk, means the polarization will be along the major axis of the disk. This polarization reversal was first illustrated in an inclined disk model by Yang et al. (2016a) (see their Figure 7;

Figure 2. Upper panel: the (signed) polarization fraction of scattered light p_s for a $45°$ inclined disk plotted against MRN-distributed dust grains with different maximum size parameters. Lower panel: the product of p_s and the albedo ω. Four vertical lines with different size parameters for an observation wavelength of $\lambda = 870\,\mu m$ are also shown. These are the maximum grain sizes for the four representative models in Section 3.2 (see Figure 3). The crosses on each of the four lines are the averaged polarization fraction in these four models, boosted by the same factor of 10 for easy comparison with the black solid curve.

see also Kirchschlager & Wolf 2014; Kataoka et al. 2015), and is the opposite of what is observed. Brunngräber & Wolf (2019) also noticed this polarization reversal in the presence of big dust grains.

The polarization fraction of the scattered light shown in the upper panel of Figure 2, however, is not the polarization fraction we observe. It will be reduced by the local unpolarized thermal emission, which depends on the local temperature, the opacity, and the column density. The ratio of the scattered light to the direct emission does not directly depend on the local column density, because both of them depend on the local column density in the same way. So roughly, the ratio of the light scattered by a dust grain to the direct thermal emission by that grain depends on the ratio between the source functions, which is $\kappa_{\rm sca}J_\nu/\kappa_{\rm abs}B_\nu$, with $\kappa_{\rm sca}$ and $\kappa_{\rm abs}$ being the scattering and absorption opacities, respectively. The J_ν is the local mean intensity, and the B_ν is the local blackbody radiation intensity. The observed polarization fraction is then, to the zeroth order, $p_s(\kappa_{\rm sca}J_\nu/\kappa_{\rm abs}B_\nu)$. The J_ν/B_ν depends on the detailed disk model, and a radiative transfer calculation is needed to determine its value. The $\kappa_{\rm sca}/\kappa_{\rm abs}$ is roughly the albedo ω of the dust grain and is solely determined by the dust model. The lower panel in Figure 2 shows the product of p_s and the albedo ω. This is very similar to Figures 3 and 4 in Kataoka et al. (2015), but our polarization fraction is averaged over radiation incident on the scatterer from different directions.

We can see that small dust grains can hardly produce any polarization due to a small albedo and the corresponding heavy dilution from direct thermal emission. As we go beyond a size parameter of order of unity, different parts of the dust grains will have different phases, which causes strong oscillations (see Tazaki et al. 2019 and their Figure 7 for an illustration), which in turn cause strong cancellation of the polarization, leading to a rapid decrease of the net polarization. This creates a peak in the distribution of the product $p_s\omega$ as a function of x, which was interpreted that the scattering-induced polarization is sensitive
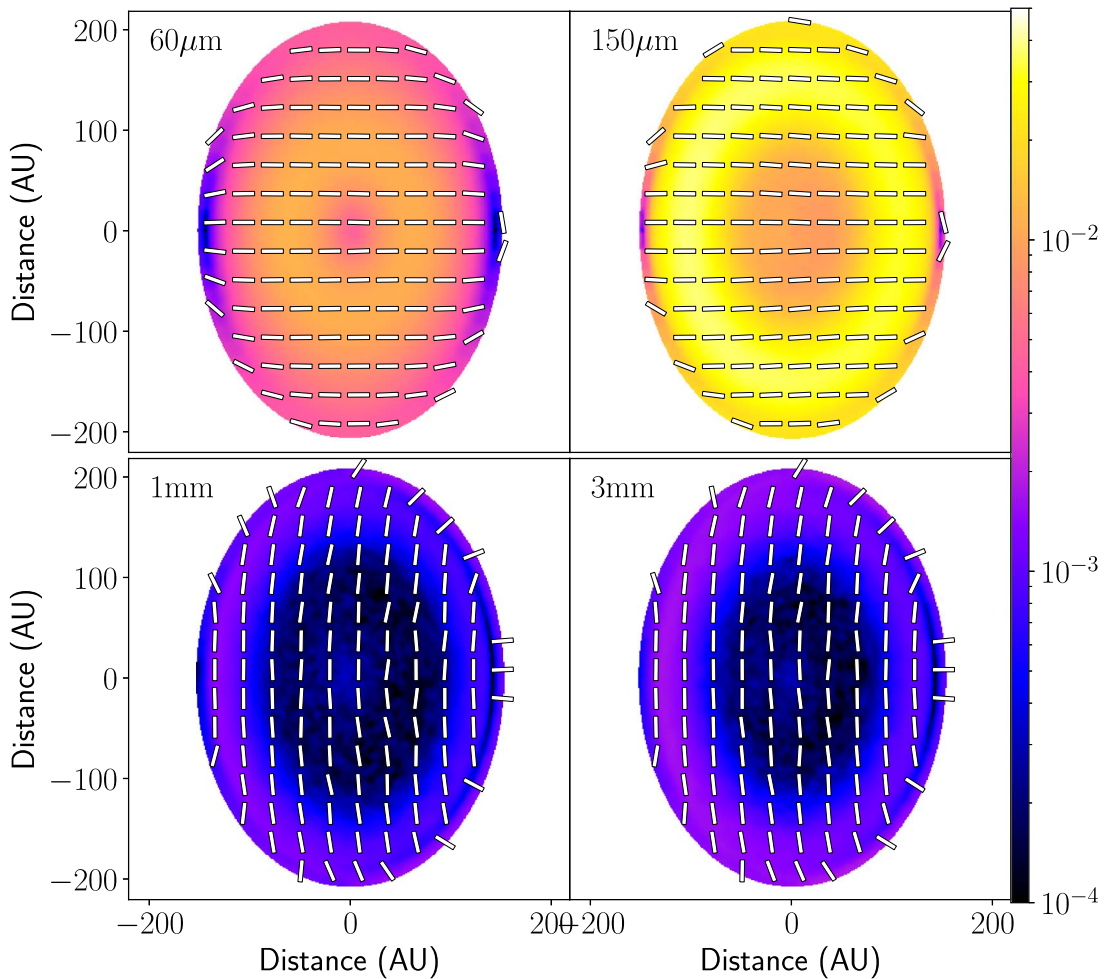
to only dust grains with size parameter on the order of unity. For ALMA Band 7, this corresponds to a grain size of about $140\,\mu m$.

For the adopted MRN size distribution with big dust grains, which includes some small dust grains with optimal sizes, the scattering is still dominated by the big ones with little polarization. If, for example, the polarization fraction near the peak of the $p_s\omega - x$ curve in the lower panel of Figure 2 is about $3\% \sim 4\%$ (based on the numerical results below; see the upper right panel of Figure 3), it would be about 0.1% for grains with size parameter of about 5 or larger. As discussed earlier, such large grains are thought to be required to produce the small opacity index β; they would have severe difficulty producing the observed disk polarization at the typical level of $\sim 1\%$.

There are two important assumptions that went into the above calculations: the grain size distribution, and the dust composition. Big dust grains with different compositions will be studied in Section 4. The adopted MRN distribution will be relaxed in Section 5.1. We also assumed compact spherical dust grains. This enables us to calculate optical properties of very large dust grains using Mie theory. Irregular or even fluffy dust grains may behave differently. Numerical calculations for these dust models, however, are very expensive and are postponed for future investigation.

3.2. Monte Carlo Calculations and Polarization Maps

In this subsection, we will verify and extend the semianalytical results presented in the last subsection using Monte Carlo simulations. For the fiducial disk model described in Section 2.2, we calculate the polarization map with different grain sizes (all with MRN distribution, characterized by its maximum grain size $a_{\rm max}$), with Monte Carlo Radiative Transfer code RADMC-3D. The results are shown in Figure 3. We can see that the polarization fraction and direction match our semianalytic results very well: big dust

Figure 3. Polarization maps at ALMA Band 7 (870 μm) for the same disk model with different maximum grain sizes: 60 μm, 150 μm, 1 mm, and 3 mm. For each panel, the color map represents the polarization fraction in logrithmic scale. The line segments represent the polarization orientation. For the adopted dust model (see text), big dust grains will produce low polarization with polarization reversal.

grains have significantly low polarization fraction. More importantly, the polarization reversal is clearly seen for the two cases with the largest maximum grain sizes (see the lower two panels of Figure 3), although such reversal may not be directly detectable with ALMA, as the polarization fraction is only 0.1%.

We also calculated the spectrum index α at wavelengths between[7] 500 μm and 3.1 mm for the whole disk for different models. Results are tabulated in Table 1. We can see that models with 1 mm maximum grain sizes or bigger have $\alpha < 3$. Under the canonical interpretations, this means $\beta < 1$ if it is optically thin radiation in the Rayleigh–Jeans limit. Our results are therefore consistent with the usual interpretation that $\beta < 1$ implies the presence of large grains.

For the adopted dust grain composition and disk model, we find that the uniform minor-axis polarization and the small spectrum index α are mutually exclusive. Uniform minor-axis polarization requires dust grains with size parameter on order of unity or smaller. At the same time, the inferred small β from small spectrum index α corresponds to big dust grains.

Table 1
Spectrum Index α (and Opacity Index β) for the Whole Disk with Different Maximum Grain Sizes a_{max} (and the Corresponding Dimensionless size Parameter x_{max})

a_{max}	x_{max}	α	$\beta (\equiv \alpha - 2)$
60 μm	0.43	3.18	1.18
150 μm	1.08	3.29	1.29
1.0 mm	7.22	2.47	0.47
3.0 mm	21.67	2.30	0.30

According to Draine (2006), a size parameter of at least ∼15 is needed to produce a $\beta \lesssim 1$. The one order difference in grain size estimates from the two methods is a tension that we seek to resolve below.

4. Polarization Phase Diagram

We have seen that the big dust grain with an oft-adopted composition cannot produce enough polarization to explain the observation. Even worse, it may cause polarization reversal, which is not firmly detected yet. In this section, we will explore different compositions of dust grains, and see if big grains can still produce the observed polarization pattern and fraction.

---

[7] This range covers the 870 μm at which the polarization is calculated. The calculated spectrum energy distributions are roughly straight lines in logrithmic plots.

4.1. The Phase Diagram

For a uniform spherical dust grain, its optical properties can be numerically calculated with the Mie theory even if it is very big, e.g., $x \sim 100$, in size. The only input required is the complex dielectric function, $\epsilon = \epsilon_r + i\epsilon_i$, or equivalently the complex refractive index, $m = n + ik$. At the same time, grains with different compositions can be approximated as a uniform medium with its dielectric function calculated through averaging their ingredients properly (the so-called "Effective Medium" method; see Bohren & Huffman 1983). As such, we can use the 2D diagram of the complex dielectric function, (n, k), to represent any compact spherical dust grain models.

Now for any point on the phase diagram, we have one type of scatterer represented by the real and imaginary components of its complex refractive index. We will then calculate the optical property of this scatterer assuming MRN distribution with maximum size parameter $x_{max} = 21.67$, which corresponds to a maximum grain size of 3 mm for ALMA Band 7. With the Muller Matrix calculated through the Mie theory (Bohren & Huffman 1983), we can evaluate Equation (5) numerically. This will give the p_s, the (signed) polarization fraction for the scattered light under the CIRF assumption. From Figure 2, we can see that the peak of the product $p_s\omega$ is between $0.15 \sim 0.2$. Numerically, one would get about $3\% \sim 4\%$ polarization for a $45°$ inclined disk of a representative mass and temperature distribution (see the upper right panel of Figure 3 for example) using optimal grain sizes. So in what follows, we will reduce the product $p_s\omega$ by a factor of 5, to account for the dilution by unpolarized direct thermal emission that is captured in our MC simulations but not by the CIRF method. This MC-calibrated product is more directly comparable to polarization observations. We should note that the calibration depends on the physical model used in the MC simulations, but the relative values for grains of different compositions should be independent of the adopted reduction factor.

Figure 4 shows the results for a wide range of complex refractive indices: $\log(n - 1)$ goes from -2 to 2 and $\log(k)$ from -3 to 2. This range covers many types of exotic materials, such as good conductors or strong insulators. The color map represents the polarization fraction in a $45°$ inclined disk. The blue part has a positive polarization, meaning that its polarization is along the minor axis of the disk. We can see that models with big absorptive dust grains can still produce positive polarization with appreciable degree (close to 1 percent). There is also region in the parameter space colored in red. Models with dust grains lying in these regions produce negative polarization (polarization along major axis), which we call "polarization reversal." Contours with selected values of the polarization fraction are also plotted.

To help with the interpretation, we overplot on the phase diagram some dots for the refractive indices for different dust grains models with different compositions at ALMA Band 7 (870 μm). Their references and brief descriptions are tabulated in Table 2. For dust models based on mixture of components, the dielectric functions are averaged using Bruggleman rule (Bohren & Huffman 1983; Birnstiel et al. 2018). The dsharp dot represents the composite dust grains used in Section 3 above. We can see that it lies in the region colored in red with polarization reversal (see above). There are four components for this DSHARP mixture: refractory organics, troilite, water ice, and astronomical silicate. We can see that the refractory

organics is the main reason for this polarization reversal: it lies deeply in the red region. Pure astrophysical silicate does not have polarization reversal, but it is polarization fraction is small. In the upper right corner of the phase diagram lies a couple of dots representing various absorptive carbonaceous dust grains. To produce moderate polarization ($>0.5\%$) using big grains, one need a large fraction of such absorptive dust grains.

5. Discussion

5.1. Different Size Distributions

One assumption in our work so far is the MRN dust size distribution. It was originally derived for small grains in the interstellar medium (Mathis et al. 1977). As such, it is the most widely adopted assumption for grain size distributions. However, there is no direct evidence that the dust grains in protoplanetary disks should follow this distribution as well. Some authors have suggested a shallower distribution. For example, Birnstiel et al. (2012) suggested a complex size distribution with multiple transition points which is meant to be a steady-state solution to the grain coagulation problem (see also Birnstiel et al. 2018). Near the maximum grain size, this distribution also suggests a shallower grain size distribution.

To study different size distributions, we first replace the MRN assumption with a more general power law $n(a) \propto a^{-q}$. Both the minimum and maximum grain sizes are fixed, with $a_{min} = 0.1\,\mu$m and $a_{max} = 3$ mm. Figure 5 shows the p_s for different power-law indices. We can see that as we increase the index q, the polarization becomes more positive and eventually overcoming the "polarization reversal" because of the larger contribution from small grains. The peak of the observable polarization, indicated by the value of $p_s\omega$, reaches its maximum around $q = 4.5$ with an MC-calibrated polarization fraction ($p_s\omega/5$, as in Section 4) of only $\sim 0.25\%$. We can see that one need to have a much steeper power law to suppress the polarization reversal and produce a reasonable polarization fraction.[8] This is expected because one need to have large fraction of small dust grains ($x \sim 1$) to produce the desired polarization degree and pattern. A steeper power law is a natural way to satisfy this requirement.
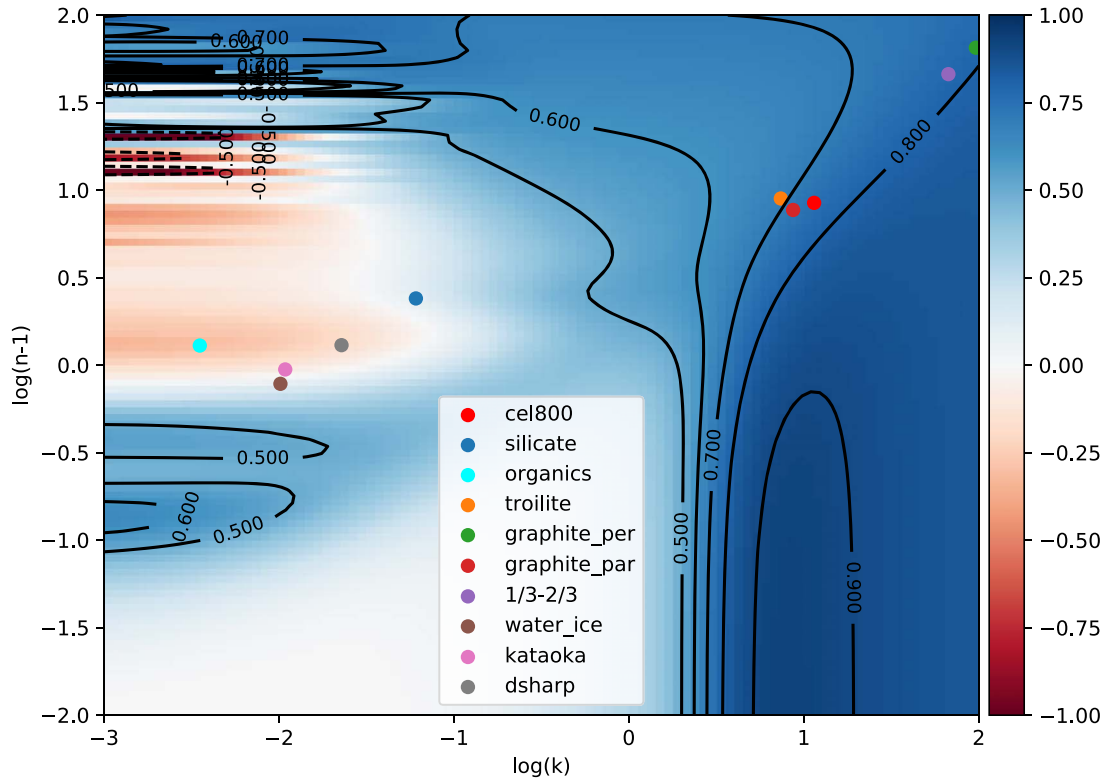
5.2. An Illustrative Model and Polarization at Longer Wavelengths

In Section 4, we see that pure absorptive carbonaceous dust grains can potentially produce the desired polarization with big grain sizes. In this subsection, we will check this conclusion with our fiducial disk model and discuss its implications.

As an illustrative model, we use the same density and temperature profile described in Section 4. For the dust grain, we use pure amorphous carbonaceous dust grains (Jager et al. 1998) with an MRN distribution. This dust grain is synthesized in a lab through pyrolyzing cellulose materials at $800°$ C. It contains 85.5%, 11.9%, and 2.6% of Carbon, Hydrogen, and Oxygen atoms, respectively. The dielectric function was measured and reported up to $\sim 500\,\mu$m and extrapolated to obtain dielectric function at (sub)millimeter wavelengths. With the maximum grain size set to 3 mm, we calculate the

---

[8] Note that such a steep distribution will have its mass dominated by small particles. In this case, the minimum size parameter may play an important role in the result, but exploring the role in detail is beyond the scope of this paper.

Figure 4. Polarization phase diagram for grains of different optical properties. The dust grains are MRN-distributed with a maximum grain size of 3 mm and the observing wavelength is ALMA Band 7 (870 μm). Each point on the map represents compact uniform grains with that effective complex refractive index $m = n + i$ k, and the map is presented with $\log_{10}(k)$ and $\log_{10}(n - 1)$ as two axes. The color map is polarization percentage (in %). Blue values represent positive polarization fraction, i.e., polarization along minor axis, or the "normal" polarization orientation. Red values represent negative polarization fraction, i.e., polarization along major axis, or the "reversed" polarization orientation. Several representative dust compositions are marked on the map based on their refractive indexes at this wavelength. More detailed description of the dust models is given in Table 2. An inclination angle of 45° is assumed.

polarization from this disk at an inclination angle of 45° at the ALMA Band 7 (870 μm) and Band 3 (3.0 mm), as shown in Figure 6.

We can see that the polarization is fairly uniform at ALMA Band 7 with no polarization reversal (see Figure 6), unlike the previous models with big dust grains of DSHARP composition (see Figure 3, lower panels) at the same (relatively short) wavelength. The polarization fraction is about 0.6% ∼ 1% across the disk, which is at the same level as the one observed in HL Tau Band 7 (Stephens et al. 2017). The spectrum energy distribution was also calculated for the whole disk between 500 μm and 3.1 mm, and the fitted spectral energy distribution power-law index α is 2.12. The inferred opacity index $\beta = 0.12$ is indeed smaller than 1. We can see that this model can indeed produce a reasonable polarization degree and pattern at ALMA Band 7 while having a small opacity index.

This model is only an illustrative model. Pure carbonaceous dust grains are not very realistic. In reality, it is possible that certain mixture of dust compositions will have its effective refractive index lie within the blue region of the phase diagram (Figure 4). It is also possible that big irregular/fluffy dust grains will behave differently than what the Mie theory predicts for compact dust grains. And they may lie effectively in the blue regions, even though their complex refractive index does not belong there. All these possibilities are very interesting to explore and we will postpone them to future investigations.

Another feature of this model is that it predicts a polarization pattern at ALMA Band 3 (∼3 mm; see the lower panel of Figure 6) that is similar to that at Band 7 (i.e., both along the

minor axis and at percent level). This similarity is observed in the disk of RY Tau, for which the polarization data at Band 3 has been published (Harrison et al. 2019; see the bottom-right panel of their Figure 1) and that at Band 7 is being prepared for publication (R. Harrison et al. 2020, in preparation). However, this predicted similarity is not seen in other disks, particularly HL Tau and DG Tau, where the polarization at Band 3 has a pattern that is predominantly azimuthal (Kataoka et al. 2017, Harrison et al. 2019), with a global net polarization fraction along the minor axis that is well below that given in Figure 6 (see Figure 4 of Kataoka et al. 2017 for HL Tau). For these sources, the more commonly adopted smaller (0.1 mm-sized) grains appear more suitable than large (mm-sized) grains in reproducing the Band 7 polarization without over-predicting a net polarization along the minor axis at Band 3. Of course, the smaller grains have the disadvantage of not being able to produce a relatively low opacity index β, which is the main motivation for exploring the scattering by large grains in the first place. In addition, neither the 0.1 mm-sized nor mm-sized grains have been shown to be capable of producing the azimuthal polarization observed in the HL disk at Band 3 through scattering alone; additional mechanism(s) appear to be required, as discussed in Kataoka et al. (2017) and Yang et al. (2019). If the mm-sized grains are aligned, there is some possibility of explaining the multi-wavelength polarization observations of HL Tau (and the relatively low spectral index) simultaneously through a combination of polarized thermal emission and scattering. One way to achieve this is to have bigger grains be better aligned. Draine & Fraisse (2009)

Table 2
Representative Dust Compositions in Figure 4

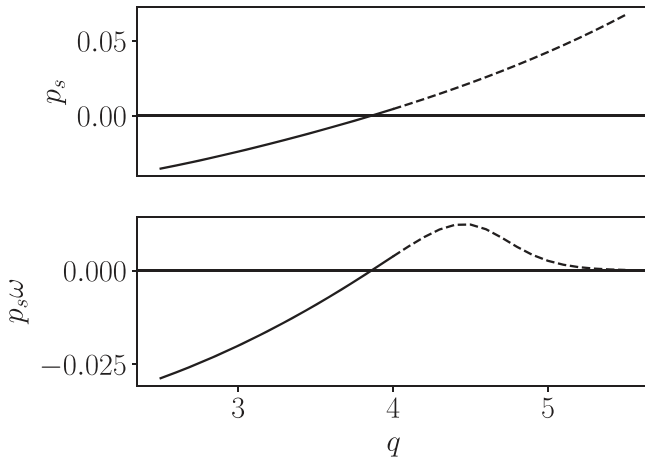| Notation	n	k	Description	Reference
cel800	9.456	11.46	Amorphous carbonaceous dust generated in lab[a]	(a)
silicate	3.404	0.0607	Astronomical Silicate	(b)
organics	2.293	0.00353	Refractive organics, the so-called "CHON" particles	(c)
troilite	9.954595	7.3896	Troilite	(c)
graphite_per	66.14	96.2	Graphite for E perpendicular to the c-axis[b]	(b)
graphite_par	8.7	8.688	Graphite for E parallel to the c-axis	(b)
1/3-2/3	46.99	67.03	Randomly oriented graphite	(b), (d)
water_ice	1.782	0.0102	Water ice	(e)
kataoka	1.944	0.0109	A mixture of dust with organics, silicate and water ice	(f), (g)
dsharp	2.300	0.0228	The DSHARP mixture[c]	(h), (b), (i), (j)

Notes. The columns list, respectively, the notations used in the legend of Figure 4, the real and imaginary part of the complex refractive indices at 870 μm, a brief description of the composition, and references.
[a] See Section 5.2 for more detailed description.
[b] The c-axis is the axis normal to the "basal plane" of graphite.
[c] Dust composition used in the DSHARP collaboration. See Table 1 in Birnstiel et al. (2018) for more details.
References. (a) Jager et al. (1998) (b) Draine (2003) (c) Pollack et al. (1994) (d) Draine & Malhotra (1993) (e) Warren (1984) (f) Kataoka et al. (2015) (g) Yang et al. (2016a) (h) Birnstiel et al. (2018) (i) Henning & Stognienko (1996) (j) Warren & Brandt (2008).

Figure 5. Polarization fraction of scattered light p_s and its product with albedo ω as a function of the power-law index q. The dashed part represents the part with $q > 4$, where the most of the mass is in the small dust grains.

predicted a transition from no polarization to high polarization going toward longer wavelengths in dichroic thermal emission of aligned grains based on mixtures of spheroidal amorphous silicate grains, spheroidal graphite grains, and PAH particles. The transition happens around 100 μm in their specific model. It is possible to change this transition wavelength to ~1 mm by changing the grain sizes. Note that their model uses the degree of alignment f as a free function of grain sizes, although this is not backed up with detailed alignment theory. Physical justification of the alignment function f at mm/submm grain sizes is still needed. On the other hand, even if the big dust grains are perfectly aligned under some mechanisms, the scattering still cannot be neglected. Calculation of scattering by aspherical big dust grains and its implementation into radiative transfer calculation are required to model the Band 3 polarization.

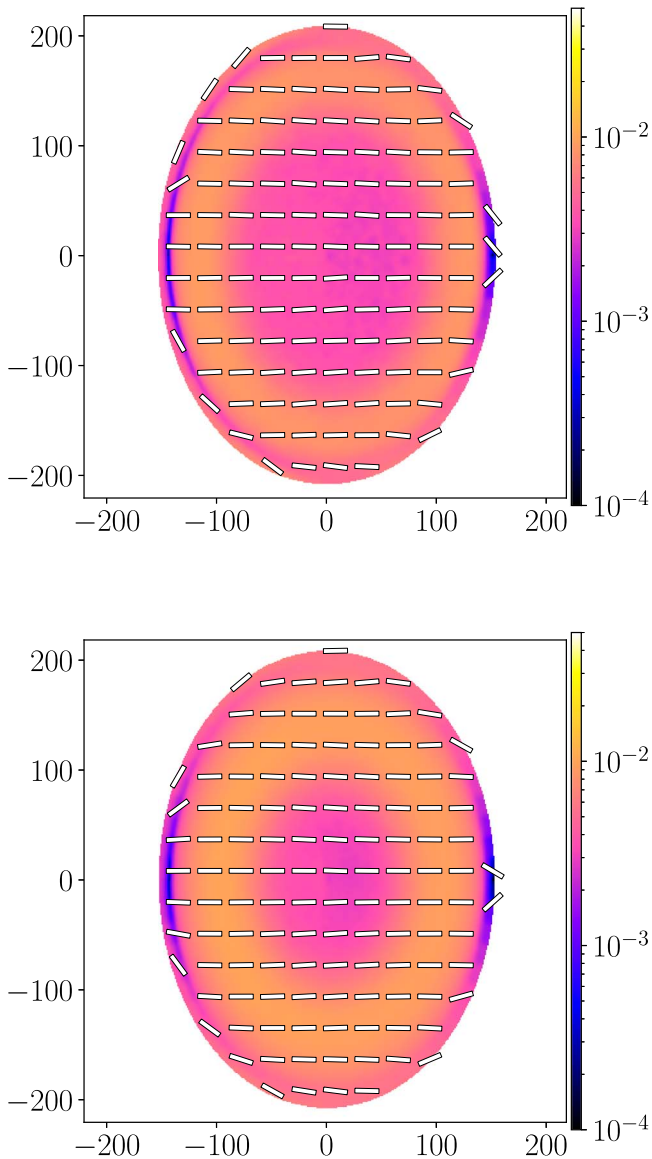### 5.3. Alternatives for Resolving the Tension in Grain Size

In this work, we adopted the conclusion from β-index measurements that the grain sizes in protoplanetary disks are big (millimeter in size or bigger). However, it is possible that the canonical conclusions from β-index method is not valid and the dust grains are indeed on the order of 100 μm. The strongest requirement for β-index method is the medium being optically thin. This assumption is likely to fail badly in protoplanetary disks at short-wavelength ALMA bands, especially at submillimeter wavelengths. Even though DSHARP survey showed that all their samples are moderately optically thin, Zhu et al. (2019) pointed out that the conclusion could be wrong and too small by potentially several orders of magnitude if the albedo of the dust grains is very high. The dimming of the disk by scattering has consequences for the observed spectral index α (and thus the inferred opacity index β as well), which complicates the picture even further (see also Liu 2019).

The finding that the grain sizes are about 100 μm from all scattering-based polarization studies to date appears to require considerable fine-tuning. One would naturally ask: why are the grain sizes always on the order of 100 μm? This question was in part answered by Okuzumi & Tazaki (2019), who used the experimental results from Musiolik et al. (2016a, 2016b) that the CO_2 ice mantled dust grains are less sticky and thus yield smaller fragmentation barrier to produce a distribution of dust grains with mostly 100 μm in size in the outer part of the HL Tau disk. The polarization map would fit the observation this way as a natural outcome. This tuning in fragmentation barrier changes our canonical understanding and need to be investigated in more detail.

Models with grain sizes capped at 100 μm also put some constraints on the planet-disk interaction. The first well-resolved protoplanetary disk image of the HL Tau system from ALMA long baseline campaign shows a very beautiful disk with rings and gaps (ALMA Partnership et al. 2015). At places, the contrast between rings and gaps could be a factor of a few or even a factor of 10. If we believe this is thermal emission of 100 μm dust grains, there should be a similar contrast between rings and gaps for the gas component as well, because 100 μm dust grains are expected to have relatively small Stokes numbers[9] and are thus expected to be well-mixed

---

[9] For a rotating disk, the Stokes number can be expressed as St = $\rho_s a/\Sigma$, where Σ is the column density for gas. For the adopted disk model prescribed by Equation (7), the Stokes number for 100 μm dust grains is on the order of 5×10^{-4}–10^{-2}, depending on the location in the disk.

Figure 6. Illustrative model of the scattering-induced polarization in an inclined disk by large pure carbonaceous dust grains at 870 μm (upper panel) and 3.0 mm (lower panel). It can produce the polarization pattern commonly observed at ALMA Band 7, while having a small opacity index β. The pattern at Band 3 is observed in some sources but not in others (see text for discussion).

with gas. The depth of the gap opened by a planet depends on various physical properties (see e.g., Zhang et al. 2018), such as the mass of the planet, the scale height of the disk, the viscosity in the disk. A factor of 10 depletion of the gas component in the gap would put a strong constraint on the allowed parameter space of a planet-disk interaction system.

6. Summary

In this work, we have studied the scattering-induced polarization in inclined disks with grains of different sizes, particular big grains. Our main results are summarized as follows:

1. We developed a semianalytical model under the Coplanar Isotropic Radiation Field approximation. It calculates the polarization fraction in scattered light from a particle

sitting at the center of an inclined geometrically thin disk. This model only requires the Muller Matrix of the dust as an input. It does not require detailed radiative transfer and is thus ideal for exploring large parameter space efficiently.

2. With an oft-adopted dust composition, we calculated the polarization fraction of scattered light in an inclined disk with 45° inclination angle with different grain sizes under the CIRF approximation. We found that for large dust grains with size parameter $x > 1$, the polarization fraction is very low, and the signed polarization becomes negative, implying that polarization is along the major (rather than minor) axis of the disk, and is thus reversed. There is, however, no clear observational evidence for such polarization reversal in protoplanetary disks to date.

3. For four representative grain sizes, we calculated the polarization maps with Monte Carlo Radiative Transfer. The polarization fractions and orientations match our expectations from the analytical CIRF model well: dust grains with size parameter of one or smaller have the desired polarization degree and orientation; models with big dust grains have very low polarization fraction and reversed polarization orientations. We also calculated the spectrum energy index α and the corresponding opacity index β. In our models, big dust grains are required to produce small β index. From these results, we conclude that uniform polarization along minor axis and small β index are mutually exclusive (assuming canonical dust compositions and compact spherical geometry).

4. To alleviate the above tension, we explored a wide range of dust properties, parameterized by the complex refractive index $m = n + ik$ (Figure 4) under the CIRF approximation, focusing on MRN size distribution with a maximum grain size of 3 mm and ALMA Band 7 (870 μm). We find that there is a parameter region that shows polarization reversal. The oft-adopted dust models fall in this region and thus fail to explain both the observed polarization map and opacity index. We find that the refractory organics are responsible for such polarization reversal.

5. On the phase diagram, we find more absorptive dust models (with bigger imaginary part of dust grains) can produce the desired polarization in both fraction and orientation with big dust grains. As an illustration, we calculated the polarization at 870 μm and 3.0 mm for a model with pure absorptive carbonaceous dust grains with maximum grain size of 3 mm (Figure 6). The polarization pattern at 870 μm is uniformly oriented along the minor axis and the polarization fraction is 0.6% ∼ 1.0%. The inferred opacity index β is also small (0.12). In this model, the tension between the often observed scattering-induced polarization along the minor axis and the small β index is resolved. The model predicts a polarization at 3.0 mm that is similar to that at 870 mum, which is broadly consistent with the multi-wavelength polarization observations of RY Tau but not HL Tau and DG Tau; for the latter sources, additional mechanism(s) are required to explain their Band 3 data (particularly the azimuthal pattern). Nevertheless, this example highlights the potential for using the polarization to probe not only the sizes but also compositions of dust grains in disks.

ORCID iDs

Haifeng Yang ⓘ https://orcid.org/0000-0002-8537-6669

References

ALMA Partnership, Brogan, C. L., Pérez, L. M., et al. 2015, ApJL, 808, L3
Alves, F. O., Girart, J. M., Padovani, M., et al. 2018, A&A, 616, A56
Bacciotti, F., Girart, J. M., Padovani, M., et al. 2018, ApJL, 865, L12
Balbus, S. A., & Hawley, J. F. 1991, ApJ, 376, 214
Bertrang, G. H. M., Flock, M., & Wolf, S. 2017, MNRAS, 464, L61
Birnstiel, T., Dullemond, C. P., Zhu, Z., et al. 2018, ApJL, 869, L45
Birnstiel, T., Klahr, H., & Ercolano, B. 2012, A&A, 539, A148
Blandford, R. D., & Payne, D. G. 1982, MNRAS, 199, 883
Bohren, C. F., & Huffman, D. R. 1983, Absorption and Scattering of Light by Small Particles (New York: Wiley)
Brunngräber, R., & Wolf, S. 2019, A&A, 627, L10
Carrasco-González, C., Sierra, A., Flock, M., et al. 2019, ApJ, 883, 71
Cho, J., & Lazarian, A. 2007, ApJ, 669, 1085
Cleeves, L. I., Öberg, K. I., Wilner, D. J., et al. 2016, ApJ, 832, 110
Cox, E. G., Harris, R. J., Looney, L. W., et al. 2015, ApJL, 814, L28
Dent, W. R. F., Pinte, C., Cortes, P. C., et al. 2019, MNRAS, 482, L29
Draine, B. T. 2003, ApJ, 598, 1026
Draine, B. T. 2006, ApJ, 636, 1114
Draine, B. T., & Fraisse, A. A. 2009, ApJ, 696, 1
Draine, B. T., & Malhotra, S. 1993, ApJ, 414, 632
Dullemond, C. P., Juhasz, A., Pohl, A., et al. 2012, RADMC-3D: A Multi-purpose Radiative Transfer Tool, Astrophysics Source Code Library, ascl:1202.015
Fissel, L. M., Ade, P. A. R., Angilè, F. E., et al. 2016, ApJ, 824, 134
Flock, M., Ruge, J. P., Dzyurkevich, N., et al. 2015, A&A, 574, A68
Girart, J. M., Fernández-López, M., Li, Z.-Y., et al. 2018, ApJL, 856, L27
Gold, T. 1952, MNRAS, 112, 215
Harris, R. J., Cox, E. G., Looney, L. W., et al. 2018, ApJ, 861, 91
Harrison, R. E., Looney, L. W., Stephens, I. W., et al. 2019, ApJL, 877, L2

Henning, T., & Stognienko, R. 1996, A&A, 311, 291
Hoang, T., Cho, J., & Lazarian, A. 2018, ApJ, 852, 129
Hull, C. L. H., Yang, H., Li, Z.-Y., et al. 2018, ApJ, 860, 82
Hull, C. L. H., & Zhang, Q. 2019, FrASS, 6, 3
Jager, C., Mutschke, H., & Henning, T. 1998, A&A, 332, 291
Kataoka, A., Muto, T., Momose, M., et al. 2015, ApJ, 809, 78
Kataoka, A., Muto, T., Momose, M., Tsukagoshi, T., & Dullemond, C. P. 2016, ApJ, 820, 54
Kataoka, A., Okuzumi, S., & Tazaki, R. 2019, ApJL, 874, L6
Kataoka, A., Tsukagoshi, T., Pohl, A., et al. 2017, ApJL, 844, L5
Kirchschlager, F., & Wolf, S. 2014, A&A, 568, A103
Lazarian, A., & Hoang, T. 2007, MNRAS, 378, 910
Lee, C.-F., Li, Z.-Y., Ching, T.-C., Lai, S.-P., & Yang, H. 2018, ApJ, 854, 56
Lin, Z.-Y. D., Li, Z.-Y., Yang, H., et al. 2020, MNRAS, in press (arXiv:1912.10012)
Liu, H. B. 2019, ApJL, 877, L22
Lynden-Bell, D., & Pringle, J. E. 1974, MNRAS, 168, 603
Mathis, J. S., Rumpl, W., & Nordsieck, K. H. 1977, ApJ, 217, 425
Musiolik, G., Teiser, J., Jankowski, T., & Wurm, G. 2016a, ApJ, 818, 16
Musiolik, G., Teiser, J., Jankowski, T., & Wurm, G. 2016b, ApJ, 827, 63
Okuzumi, S., & Tazaki, R. 2019, ApJ, 878, 132
Pattle, K., & Fissel, L. 2019, FrASS, 6, 15
Pérez, L. M., Carpenter, J. M., Chandler, C. J., et al. 2012, ApJL, 760, L17
Pérez, L. M., Chandler, C. J., Isella, A., et al. 2015, ApJ, 813, 41
Pinte, C., Dent, W. R. F., Ménard, F., et al. 2016, ApJ, 816, 25
Planck Collaboration, Ade, P. A. R., Aghanim, N., et al. 2015, A&A, 576, A104
Pollack, J. B., Hollenbach, D., Beckwith, S., et al. 1994, ApJ, 421, 615
Stephens, I. W., Looney, L. W., Kwon, W., et al. 2014, Natur, 514, 597
Stephens, I. W., Yang, H., Li, Z.-Y., et al. 2017, ApJ, 851, 55
Tazaki, R., Tanaka, H., Muto, T., Kataoka, A., & Okuzumi, S. 2019, MNRAS, 485, 4951
Testi, L., Birnstiel, T., Ricci, L., et al. 2014, in Protostars and Planets VI, ed. H. Beuther et al. (Tucson, AZ: Univ. Arizona Press), 339
Warren, S. G. 1984, ApOpt, 23, 1206
Warren, S. G., & Brandt, R. E. 2008, JGRD, 113, D14220
Yang, H., Li, Z.-Y., Looney, L., & Stephens, I. 2016a, MNRAS, 456, 2794
Yang, H., Li, Z.-Y., Looney, L. W., et al. 2016b, MNRAS, 460, 4109
Yang, H., Li, Z.-Y., Looney, L. W., Girart, J. M., & Stephens, I. W. 2017, MNRAS, 472, 373
Yang, H., Li, Z.-Y., Stephens, I. W., Kataoka, A., & Looney, L. 2019, MNRAS, 483, 2371
Zhang, S., Zhu, Z., Huang, J., et al. 2018, ApJL, 869, L47
Zhu, Z., Zhang, S., Jiang, Y.-F., et al. 2019, ApJL, 877, L18